

Taylor dispersion of elongated rods

Ajay Harishankar Kumar,¹ Stuart J. Thomson,¹ Thomas R. Powers,^{1,2} and Daniel M. Harris^{1,*}

¹*Brown University, Center for Fluid Mechanics and School of Engineering, 184 Hope St., Providence RI 02912.*

²*Brown University, Brown Theoretical Physics Center and Department of Physics, 184 Hope St., Providence RI 02912.*

(Dated: November 11, 2020)

Particles transported in fluid flows, such as cells, polymers, or nanorods, are rarely spherical. In this study, we numerically and theoretically investigate the dispersion of an initially localized patch of passive elongated Brownian particles constrained to one degree of rotational freedom in a two-dimensional Poiseuille flow, demonstrating that elongated particles exhibit an enhanced longitudinal dispersion. In a shear flow, the rods translate due to advection and diffusion and rotate due to rotational diffusion and their classical Jeffery's orbit. The magnitude of the enhanced dispersion depends on the particle's aspect ratio and the relative importance of its shear-induced rotational advection and rotational diffusivity. When rotational diffusion dominates, we recover the classical Taylor dispersion result for the longitudinal spreading rate using an orientationally averaged translational diffusivity for the rods. However, in the high-shear limit, the rods tend to align with the flow and ultimately disperse more due to their anisotropic diffusivities. Results from our Monte Carlo simulations of the particle dispersion are captured remarkably well by a simple theory inspired by Taylor's original work. For long times and large Peclet numbers, an effective one-dimensional transport equation is derived with integral expressions for the particles' longitudinal transport speed and dispersion coefficient. The enhanced dispersion coefficient can be collapsed along a single curve for particles of high aspect ratio, representing a simple correction factor that extends Taylor's original prediction to elongated particles.

I. INTRODUCTION

Understanding the transport of particles in fluid flow has led to the development of novel particle separation techniques, mixing strategies, and lab-on-a-chip devices [1, 2]. In many practical cases of interest, the geometry of the particles themselves may be complex [3], and hence it is important to understand how their shape [4] influences their bulk transport. Herein, we study how the elongated shape of passive, rod-like Brownian particles affects their dispersion in a steady, two-dimensional Poiseuille flow.

In a seminal paper [5], Taylor quantified the dispersion of spherical solute particles subject to Poiseuille flow in a cylindrical pipe. In Taylor's original physical picture (see Figure 1), when a uniform patch of a solute is injected in a laminar flow, it spreads due to the combined effects of advection and diffusion. At early times, a solute patch mimics the shape of the parabolic flow profile, inducing lateral concentration gradients that drive net lateral transport by molecular diffusion. Ultimately, the shear flow enhances the spreading of the solute, a phenomenon now known as Taylor dispersion. Later, Aris expanded on Taylor's results in more rigorous mathematical detail using the method of moments, and thus this phenomenon is also frequently referred to as Taylor-Aris dispersion [6]. Perhaps the most complete mathematical treatment is due to Frankel & Brenner [7], who derived a generalized theory of Taylor-Aris dispersion. This robust framework has since been used to solve a wide class of dispersion problems, including the dispersion of active matter systems in shear flow [8–11]. Of most relevance to the present work, Peng and Brady studied the upstream swimming and dispersion of active Brownian particles in a two-dimensional Poiseuille flow with one degree of rotational freedom for spherical and rod-shaped particles, demonstrating enhancement of the dispersion factor for active Brownian particles due to their swimming (i.e. activity) [12]. Such an enhancement was observed experimentally for bacteria in porous media [13]. Elsewhere, the effect of channel geometry on the dispersion of passive tracers has been well-documented to control or enhance the dispersion properties [14–16], while the effect of the dispersion factor on pulsatile flow has also been documented [17, 18]. Previous studies have also focused on the Brownian motion of ellipsoidal [19, 20] and boomerang-shaped particles [21] in the absence of external flow. However, despite these advances, the effect of a passive particle's shape on dispersion in the presence of flow has received relatively little attention.

It is now well-known that confined rod-shaped particles or fibres have the tendency to migrate towards channel walls when subject to a background shear flow [22–26]. This effect was characterized by Nitsche & Hinch [27], who studied the lateral migration velocity and resultant distribution of rod-shaped particles in quasi-two-dimensional

* daniel_harris3@brown.edu

shear flow, assuming a uniform particle concentration in the longitudinal direction. In complement to this prior work, we characterize the *longitudinal* transport properties of an initial concentration of confined Brownian rods in two-dimensional Poiseuille flow, using both Monte Carlo simulations and theoretical considerations. The rods are non-interacting Brownian tracers and modeled as elongated ellipsoids, neglecting any wall-based hydrodynamic effects. Our study reveals and quantifies two main results: a reduced mean transport speed for the rods compared to the mean speed of the fluid, and an enhanced rate of longitudinal dispersion compared to spherical particles.

As it pertains to the results presented herein, in the remainder of this section, we review Taylor's classical analysis applied to spherical particles in two-dimensional Poiseuille flow [5], followed by a discussion of extra physical considerations relevant for elongated particles. In §II, we describe our Monte Carlo method for calculating the dispersion coefficient for ellipsoidal particles in a two-dimensional Poiseuille flow. We then turn to a simplified theoretical analysis in the spirit of Taylor's original calculation in §III, deriving semi-analytical expressions for the mean speed of the particles and the dispersion coefficient, in excellent agreement with the Monte Carlo simulations. We conclude with a summary of our results in §IV.

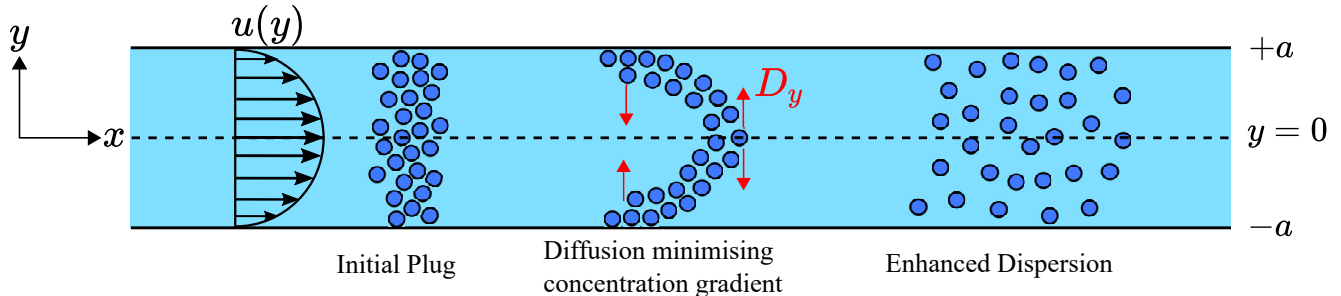


FIG. 1. Illustration of the classical Taylor dispersion process. At early times a plug of non-interacting Brownian tracer particles mimics the shape of the flow. The shear flow induces lateral concentration gradients that molecular diffusion tends to minimize. The overall effect is an enhanced diffusive-like longitudinal spreading of particles as the solute patch is advected downstream at the mean speed of the fluid flow.

Consider a parallel plate channel separated by a distance of $2a$ with a fully developed Poiseuille flow with a maximum velocity of U at $y = 0$, as depicted in Figure 1. For isotropic solute particles with a characteristic diffusion constant D , a diffusive time scale can be defined as $t_d = a^2/D$, which is the characteristic time for a solute particle to travel from the center of the channel to the walls purely through molecular diffusion. There are two primary mechanisms of particle transport in this problem, namely advection and diffusion, and the Peclet number characterizes the relative importance of advective to diffusive transport

$$\text{Pe} = \frac{Ua}{D}. \quad (1)$$

For long times $t \gg t_d$ and large Pe , Taylor characterized the laterally averaged concentration profile $\bar{C}_m(x, t)$ with an effective dispersion constant κ_s that depends on the properties of the flow, channel geometry, and particles [5]. Taylor's original calculation was performed for a circular pipe, but the same analysis can be readily applied to describe dispersion in a two-dimensional channel (i.e. infinite parallel plates). Non-dimensionalizing time using the diffusive time, t_d , and x and y with the half-width of the channel, a , it can be shown that the non-dimensional form of the laterally averaged transport equation for the two-dimensional channel can be described by the one-dimensional advection-diffusion equation

$$\frac{\partial \bar{C}_m}{\partial t} + \frac{2}{3}\text{Pe} \frac{\partial \bar{C}_m}{\partial x} = \kappa_s \frac{\partial^2 \bar{C}_m}{\partial x^2}, \quad (2)$$

where the effective dispersion constant is

$$\kappa_s = \frac{16}{945}\text{Pe}^2, \quad (3)$$

or, in dimensional form,

$$\kappa'_s = D\kappa_s = \frac{16}{945} \frac{U^2 a^2}{D}. \quad (4)$$

When the Peclet number, Pe , is large, equation (3) or (4) implies a significant increase in the longitudinal spreading rate due to the presence of the parallel shear flow. We also note from equation (4) that the effective dispersion coefficient is in fact *inversely* related to the molecular diffusion constant of the particle. In Taylor's analysis, the contribution of molecular diffusion to the expression for the effective dispersion, κ_s , arises strictly from the lateral (y) diffusion term in the advection-diffusion equation governing the concentration of particles. Thus, in scenarios where the diffusion may be anisotropic (for example, when the solute particles are non-spherical, or when the diffusivity depends on y), the lateral diffusion coefficient, D_y , is the appropriate value to consider in such a scaling to estimate the effective dispersion constant. We will now discuss important quantities pertaining to ellipsoidal particles in a fluid.

The diffusion constants for an ellipsoidal particle constrained to translate and rotate in a plane follow from the Stokes-Einstein relation [19, 20, 28]. Rotational and translational diffusion for an ellipsoidal particle are decoupled due to its symmetry [29–31]. The translational diffusion constants D_{\parallel} and D_{\perp} for a prolate ellipsoid are indicated in Figure 2, and are given by [32, 33]

$$D_{\parallel} = \frac{k_b T}{16\pi\mu b_p} \left[-\frac{2p}{p^2 - 1} + \frac{2p^2 - 1}{(p^2 - 1)^{3/2}} \log \left(\frac{p + \sqrt{p^2 - 1}}{p - \sqrt{p^2 - 1}} \right) \right], \quad (5)$$

$$D_{\perp} = \frac{k_b T}{16\pi\mu b_p} \left[\frac{p}{p^2 - 1} + \frac{2p^2 - 3}{(p^2 - 1)^{3/2}} \log \left(p + \sqrt{p^2 - 1} \right) \right], \quad (6)$$

where k_b is Boltzmann's constant, T is temperature, $p \equiv a_p/b_p$ is the ratio of the semi-major and semi-minor axes of the particle, and μ is the dynamic viscosity. Note that for prolate ellipsoids, $p > 1$, and $D_{\parallel} \rightarrow 2D_{\perp}$ in the "slender-body" limit $p \rightarrow \infty$. An orientationally averaged diffusivity can be computed as

$$\bar{D} = \frac{D_{\perp} + D_{\parallel}}{2}. \quad (7)$$

Figure 3(a) shows how D_{\perp} and D_{\parallel} depend on the aspect ratio. A particle diffuses more readily along its long axis than against it. The rotational diffusion constant is [34, 35]

$$D_{\theta} = \frac{3k_b T}{16\pi\mu b_p^3} \frac{p}{p^4 - 1} \left[\frac{(2p^2 - 1) \log \left(p + \sqrt{p^2 - 1} \right)}{p\sqrt{p^2 - 1}} - 1 \right]. \quad (8)$$

Equations (5), (6) and, (8) are commonly used to study the Brownian motion of ellipsoids confined to one degree of rotational freedom [19, 20].

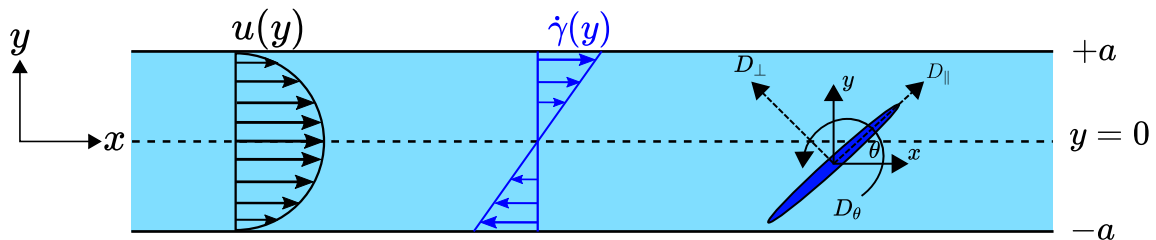


FIG. 2. Schematic of a channel with the distance between the plates equal to $2a$ with a parabolic Poiseuille flow $u(y)$ and shear rate $\dot{\gamma}(y)$. The figure also depicts the coordinate axes for each particle in the channel and its diffusivities.

Ellipsoidal particles rotate in a shear flow with a non-uniform rotational velocity in so-called Jeffery's orbits [36]. For a prolate spheroid confined to one degree of rotational freedom in the plane within a two-dimensional Stokes flow, the rotation rate ω is a function of its angle θ relative to the flow [37]

$$\omega(\theta) = \dot{\gamma} \frac{p^2 \sin^2 \theta + \cos^2 \theta}{p^2 + 1}, \quad (9)$$

where $\dot{\gamma}$ is the local shear rate. Note in the slender-body limit ($p \rightarrow \infty$), the expression of the rotation rate reduces to $\omega(\theta) = \dot{\gamma} \sin^2 \theta$. Equation (9) is plotted in Figure 3(b) and shows that elongated particles ($p > 1$) rotate fastest along the direction of the flow and rotate slowest normal to the direction of flow. Therefore, rods tend to spend more

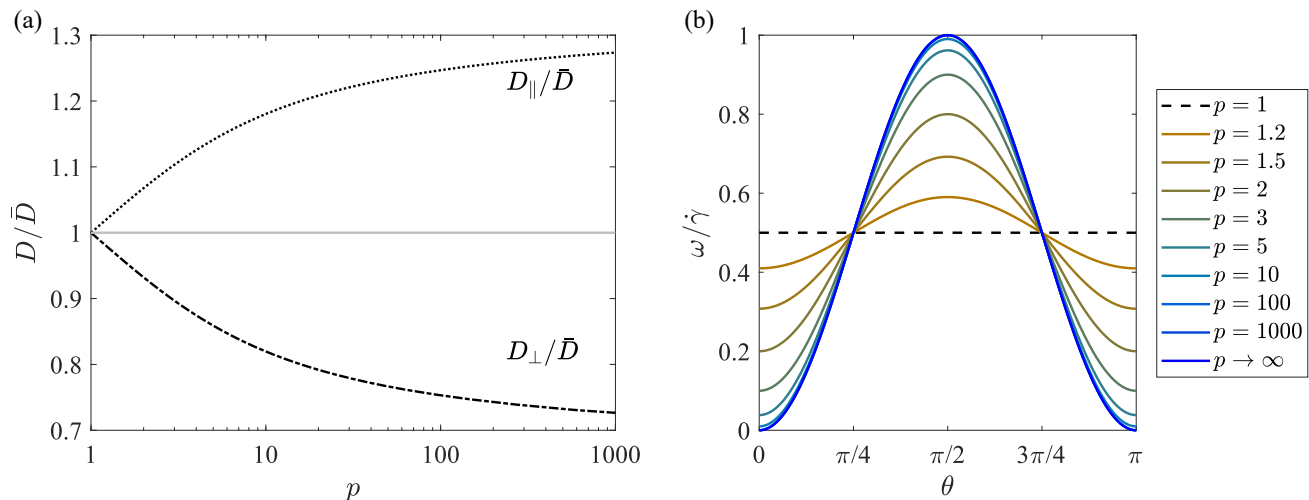


FIG. 3. (a) Plot of D_{\perp}/\bar{D} (dash-dotted curve) and D_{\parallel}/\bar{D} (dotted curve). (b) The rotation rate for different aspect ratios as a function of the angle θ between the rod axis and the flow direction. In the absence of Brownian motion, the rods rotate the fastest when aligned normal to the direction of flow and rotate most slowly when aligned in the flow direction, spending more time in each revolution aligned with the flow.

time aligned with the flow during a complete orbit. For a parabolic velocity profile, the shear rate is a linear function across the channel with the largest magnitude at the walls, as depicted in Figure 2. The rotational degree of freedom prompts us to define a rotational Peclet number

$$\text{Pe}_r = \frac{U}{aD_{\theta}}, \quad (10)$$

which is the ratio of the shear rate to rotational diffusion. For the case of a linear Couette shear flow, previous work has focused on describing how weak Brownian motion affects the three-dimensional Jeffery orbits [38], and more recent work has explored the purely rotational analog of Taylor dispersion in which shear leads to a higher dispersion coefficient for rotation [39, 40]. As mentioned previously, for the case of a Poiseuille flow, ellipsoidal particles (unlike spherical particles) are known to migrate to the channel walls due to anisotropic diffusivity and different alignments at different local shear rates [22, 25–27].

II. MONTE CARLO SIMULATION

In this section, we model the dynamics of individual Brownian rods subjected to a fluid flow to deduce macroscopic statistical quantities using Monte Carlo simulation. The results uncover the presence of an enhanced dispersion for elongated particles, and allow us to establish a simple physical picture for the phenomenon and its parametric dependencies.

A. Method

We employ a Monte Carlo method for simulating the statistics of the translational and rotational motion and for computing the dispersion coefficient and mean speed of the particles for ellipsoidal particles in a two-dimensional channel with Poiseuille flow defined by

$$\mathbf{u}(y) = U \left[1 - \left(\frac{y}{a} \right)^2 \right] \hat{x} = u(y) \hat{x}, \quad (11)$$

as depicted in Figure 2. We write the governing equations as stochastic differential equations since these equations directly correspond to our numerical approach (see also [15]), but our equations could equally well be written in

Langevin form [19]. The translational displacements of the particle in the laboratory frame are given by

$$dx = u(y(t))dt + \sqrt{2D_{\parallel}}dW_{\parallel} \cos \theta(t) - \sqrt{2D_{\perp}}dW_{\perp} \sin \theta(t) \quad (12)$$

$$dy = \sqrt{2D_{\parallel}}dW_{\parallel} \sin \theta(t) + \sqrt{2D_{\perp}}dW_{\perp} \cos \theta(t). \quad (13)$$

The white noise increments dW_{\perp} and dW_{\parallel} have zero mean, variance \sqrt{dt} , and are independent at different times. Similarly, the stochastic differential equation for the particle orientation is

$$d\theta = \omega(y(t), \theta(t))dt + \sqrt{2D_{\theta}}dW_{\theta}, \quad (14)$$

with the rotational velocity given by equation (9) for the flow (11), namely

$$\omega(y, \theta) = -2U \frac{y}{a^2} \frac{p^2 \sin^2 \theta + \cos^2 \theta}{p^2 + 1}, \quad (15)$$

and with zero mean, variance dt , and white noise dW_{θ} .

We non-dimensionalize equations (11)–(15) via $\tilde{\mathbf{x}} = \mathbf{x}/a$, $\tilde{t} = t/t_d = ta^2/\bar{D}$, $\tilde{u} = u/U$, $\tilde{\omega} = \omega a/U$ and $\tilde{D} = D/\bar{D}$. Dropping the tildes, equations (12) and (14) become

$$dx = \text{Pe} u(y(t)) dt + \sqrt{2D_{\parallel}}dW_{\parallel} \cos \theta(t) - \sqrt{2D_{\perp}}dW_{\perp} \sin \theta(t) \quad (16)$$

$$dy = \sqrt{2D_{\parallel}}dW_{\parallel} \sin \theta(t) + \sqrt{2D_{\perp}}dW_{\perp} \cos \theta(t) \quad (17)$$

$$d\theta = \text{Pe} \omega(y(t), \theta(t))dt + \sqrt{2\frac{\text{Pe}}{\text{Pe}_r}}dW_{\theta}, \quad (18)$$

where $\text{Pe} = Ua/\bar{D}$ (cf. equation (1)) and $\text{Pe}_r = U/(aD_{\theta})$ (equation (10)). The initial condition for the simulation is $n = 10^6$ particles uniformly distributed across y and across all orientations θ , but with a Gaussian distribution in x of unit variance centered at $x = 0$. The particles are non-interacting and evolve independently. The boundary conditions at the walls are billiard-like. For a collision at a wall, the center-of-mass trajectory of a particle has an angle of incidence equal to the angle of reflection, and the orientation is assumed unchanged. To solve the governing equations for each particle, we use Euler time-stepping with a dimensionless time-step of $dt = 4 \times 10^{-5}$. Consequently, the typical magnitude of the white noise is therefore much less than the width of the channel, so that it is exceedingly rare for there to be more than one wall collision in a time step. Since the Monte Carlo evolution is implemented at each time step on all the particles, the code is parallelized over many CPUs to reduce computational time. The complete Monte Carlo simulation code is included as Supplemental Material.

Although it is a slow method with a convergence rate that scales with $1/\sqrt{n}$, the gridless stochastic differential equation approach is convenient for combining and capturing all statistics [41–43].

We compute ensemble averages by carrying out r runs of the motion of the n particles. For the results reported here we take $r = 100$. The time-dependent mean and the variance of the x components of all n/r particles in a given run are calculated as

$$\mu_i(t) = \frac{r}{n} \sum_{j=1}^{n/r} x_{i,j}(t) \quad \text{and} \quad \sigma_i^2(t) = \frac{r}{n} \sum_{j=1}^{n/r} (x_{i,j}(t) - \mu_i(t))^2 \quad (19)$$

and then these quantities are averaged over all runs yielding

$$\bar{\mu}(t) = \frac{1}{r} \sum_{i=1}^r \mu_i(t) \quad \text{and} \quad \bar{\sigma}^2(t) = \frac{1}{r} \sum_{i=1}^r \left(\sigma_i^2(t) + (\mu_i(t) - \bar{\mu}(t))^2 \right). \quad (20)$$

When $n \rightarrow \infty$, the mean particle speed and dispersion coefficient are given by

$$U_p = \left. \frac{d\bar{\mu}}{dt} \right|_{t \rightarrow \infty} \quad \text{and} \quad \kappa = \left. \frac{d\bar{\sigma}^2}{dt} \right|_{t \rightarrow \infty}, \quad (21)$$

respectively. In practice, there are transients in the dispersion that decay after a dimensionless time of approximately $0.25t_d$ [14, 15]. Therefore, to calculate the effective diffusivity, we fit the computed variance to an expression of the form

$$\sigma^2(t) = s - a_1(1 - e^{-a_2 t}) + \kappa t, \quad (22)$$

using a least-squares method, where $s = 1$ is the initial variance in x . Likewise, we fit the mean speed of the particles to

$$\mu(t) = b_0 + b_1 e^{-b_2 t} + U_p t, \quad (23)$$

to find the mean speed U_p at long times.

B. Results

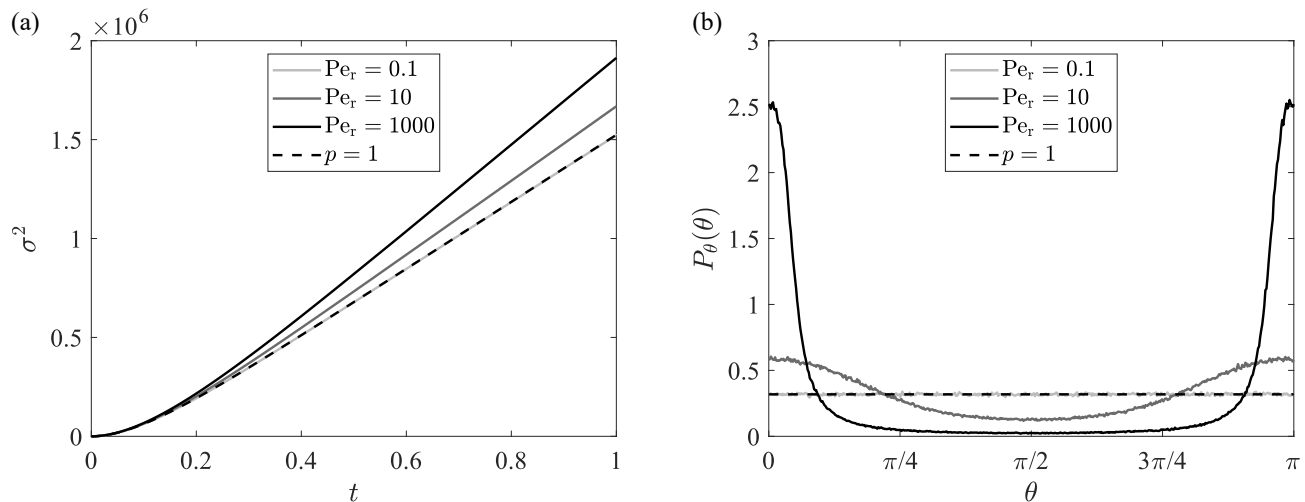


FIG. 4. (a) Monte Carlo results for the variance of the x -position of ellipsoidal particles ($p = 1000$) and spherical particles at $Pe = 10^4$ for different Pe_r as a function of dimensionless time. The rods disperse along x like spheres when rotational Brownian motion dominates ($Pe_r \ll 1$). The dispersion of rods is larger when shear dominates ($Pe_r \gg 1$), i.e., when the rods' orientations follow Jeffery orbits. The complete theoretical prediction for the variance of spherical particles in a two-dimensional channel has been reported previously and is also shown here for comparison (dashed line) [16]. (b) Monte Carlo results for the orientational distribution $P_\theta(\theta)$ for particles over the channel's length. The rods spend more time aligned with the flow direction when $Pe_r \gg 1$.

In Taylor's original picture, flow enhances spreading due to differences in the flow speed across the channel. Our simulations reveal that this enhancement is, in fact, *increased* for rod-like particles, as shown in Figure 4(a). Physically, spherical particles rotate uniformly in shear. However, rod-like particles have a non-uniform rotation rate (Figure 3(b)), and thus spend more time aligned with the flow than perpendicular to the flow. This alignment effect becomes stronger as the rotational Peclet number, Pe_r , increases (see Figure 4(b)). For small values of Pe_r , the rod shaped particles rotate randomly and spread identically to spherical particles. As the shear rate increases, the strong alignment in the direction of the flow causes the perpendicular "side" of the particles (which has a lower diffusivity than spherical particles) to diffuse across the shear layers. We can be somewhat more quantitative by noting that the effective lateral diffusivity D_y (defined more precisely in the next section) is smaller for rods than spheres. Thus, since we expect $\kappa' \propto U^2 a^2 / D_y$, and since $\kappa'_s \propto U^2 a^2 / D$, we have

$$\frac{\kappa}{\kappa_s} = \frac{\kappa'}{\kappa'_s} \sim \frac{D}{D_y}. \quad (24)$$

Our Monte Carlo results for the effective diffusivity are shown as a function of rotational Peclet number in Figure 5 for various values of the Peclet number (Figure 5(a)) and aspect ratio (Figure 5(b)). From Figure 5(a) we can conclude that the Pe^2 scaling holds for rod-shaped particles at $Pe \gtrsim 100$, as is the case for spherical particles. Figure 5(b) demonstrates that at low Pe_r , rod shaped particles behave like spherical particles as rotational diffusion dominates, and the rods are oriented randomly. Furthermore, as the Pe_r increases, we see the rods tend to align themselves in the direction of the flow due to their Jeffery's Orbit and ultimately spread more. Rods with larger aspect ratios have a stronger alignment and a lower perpendicular diffusion constant (D_\perp), and thus spread more.

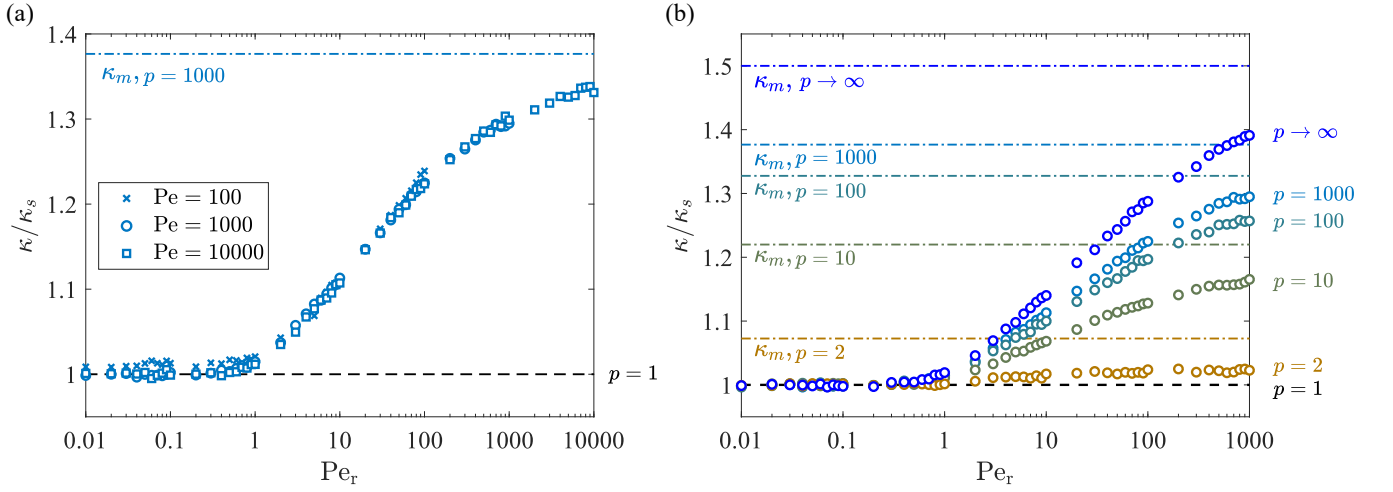


FIG. 5. (a) Effective diffusivity κ of rod shaped particles, normalized by the effective diffusivity for spheres, as a function of Pe_r for various values of Pe . The circles represent Monte Carlo simulations for $Pe = 1000$, the crosses represent $Pe = 100$, and the squares represent $Pe = 10000$. (b) Variation of normalized effective diffusivity with aspect ratio p . In both panels, the dash-dotted line represents the maximum theoretical value of dispersion for the corresponding aspect ratio. The maximum possible dispersion constant is obtained when all rod shaped particles are aligned in the direction of the flow and is defined as per equation (25).

For a given set of parameters, the maximum possible value of dispersion anticipated, κ_m , can be estimated by simply assuming all of the particles maintain perfect alignment with the flow. Thus $D_y = D_\perp$, and

$$\frac{\kappa_m}{\kappa_s} = \frac{\bar{D}}{D_\perp}. \quad (25)$$

The ratio κ_m/κ_s depends solely on the aspect ratio of the rod p , and increases monotonically from $\kappa_m/\kappa_s = 1$ when $p = 1$ (spherical particle) to $\kappa_m/\kappa_s = 3/2$ as $p \rightarrow \infty$ (slender body limit). Figure 6 shows the maximum possible dispersion as a function of the aspect ratio and allows us to define a region where we expect to find values of κ in practice.

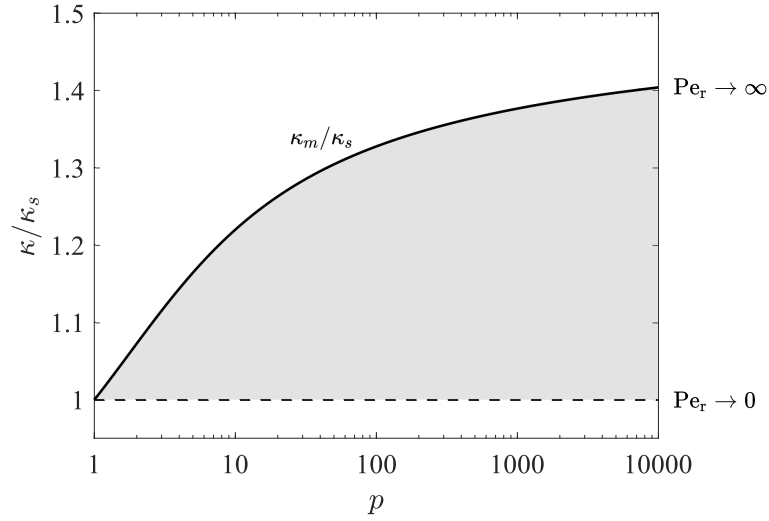


FIG. 6. The maximum possible dispersion κ_m normalized by κ_s as a function of aspect ratio p . The shaded area corresponds to the region of possible values of κ/κ_s for all p and Pe_r .

We note that the results of the Monte Carlo simulations presented here only make physical sense for $Pe_r < Pe$, as

we now describe. The ratio of Pe_r and Pe is the ratio of the rotational and translational diffusive time scales

$$\frac{\text{Pe}_r}{\text{Pe}} = \frac{\bar{D}}{a^2 D_\theta}. \quad (26)$$

where, by the Stokes-Einstein relation [28],

$$\bar{D} \sim \frac{k_b T}{\mu r_p} \quad \text{and} \quad D_\theta \sim \frac{k_b T}{\mu r_p^3}, \quad (27)$$

and r_p is the characteristic length scale of the particle. Therefore we have that

$$\frac{\text{Pe}_r}{\text{Pe}} \sim \frac{r_p^2}{a^2} \ll 1. \quad (28)$$

Since we focus on the physically relevant regime where $r_p \ll a$, this condition suggests restricting our attention to $\text{Pe}_r \ll \text{Pe}$, a fact we will exploit in the following section to derive semi-analytical expressions for the dispersion coefficient, κ , and mean particle speed, U_p .

III. THEORETICAL ANALYSIS

In this section, we generalize Taylor's continuum analysis of the dispersion of spherical particles in a shear flow to ellipsoidal particles. We write the Fokker-Planck equation for the probability density function for the particles' positions and orientations. We then use a semi-analytic asymptotic analysis to determine an effective one-dimensional transport equation with an effective dispersion coefficient and the longitudinal transport speed similar to equation (2).

A. Conservation equation: the Fokker-Planck model

We define the probability distribution $P(\mathbf{x}, \theta, t)$ via $NP(\mathbf{x}, \theta, t) = C(\mathbf{x}, \theta, t)$, where N is the total number of solute particles and $C(\mathbf{x}, \theta, t)$ is the concentration of particles with alignment angle, θ , at time, t , i.e. $C(\mathbf{x}, \theta, t)\Delta\mathbf{x}\Delta\theta$ is the number of particles in a small volume of area $d\mathbf{x}$ about $\mathbf{x} = (x, y)$ and with an alignment angle within $d\theta$ of θ . Conservation of particles implies the probability distribution obeys the Fokker-Planck equation

$$\frac{\partial P}{\partial t} + \nabla \cdot \mathbf{J} + \frac{\partial}{\partial \theta} J_\theta = 0, \quad (29)$$

where the translational flux is \mathbf{J} and the rotational flux is J_θ . Each of these fluxes has contributions from both advection and diffusion:

$$\mathbf{J} = \mathbf{u}P + \mathbf{D} \cdot \nabla P, \quad (30)$$

$$J_\theta = \omega P + D_\theta \frac{\partial P}{\partial \theta}, \quad (31)$$

with \mathbf{u} given by the flow in equation (11), and ω given by the rotation rate of the Jeffery orbit in equation (9). The diffusion tensor \mathbf{D} is given by [44]

$$\mathbf{D}(\theta) = \mathbf{e} \mathbf{e} D_{\parallel} + (1 - \mathbf{e} \mathbf{e}) D_{\perp}, \quad (32)$$

where $\mathbf{e} = (\cos \theta, \sin \theta)$. In the xy (laboratory) basis, the components of the translational diffusion tensor are

$$\mathbf{D} = \begin{bmatrix} D_{\parallel} \cos^2 \theta + D_{\perp} \sin^2 \theta & (D_{\parallel} - D_{\perp}) \sin \theta \cos \theta \\ (D_{\parallel} - D_{\perp}) \sin \theta \cos \theta & D_{\parallel} \sin^2 \theta + D_{\perp} \cos^2 \theta \end{bmatrix} = \begin{bmatrix} D_{xx}(\theta) & D_{xy}(\theta) \\ D_{xy}(\theta) & D_{yy}(\theta) \end{bmatrix}. \quad (33)$$

Thus, the conservation equation (29) can be written as

$$\begin{aligned} \frac{\partial P}{\partial t} = & -u(y) \frac{\partial P}{\partial x} + D_{xx}(\theta) \frac{\partial^2 P}{\partial x^2} + 2D_{xy}(\theta) \frac{\partial^2 P}{\partial x \partial y} \\ & + D_{yy}(\theta) \frac{\partial^2 P}{\partial y^2} + D_\theta \frac{\partial^2 P}{\partial \theta^2} - \frac{\partial}{\partial \theta} [\omega(y, \theta) P]. \end{aligned} \quad (34)$$

In addition to periodicity of P in orientational space, we specify the no-flux boundary condition at the walls

$$(\mathbf{J} \cdot \hat{y})|_{y=\pm a} = D_{yy}(\theta) \left. \frac{\partial P}{\partial y} \right|_{y=\pm a} = 0. \quad (35)$$

Inspired by Taylor's original analysis [5], in what follows we consider time-scales much longer than the time-scale for diffusion in the lateral direction, namely $t \gg t_d$. Specifically, we consider the scenario $a^2/\bar{D} \ll L^2/\bar{D}$, where L is characteristic length-scale over which longitudinal gradients in the solute concentration over the lateral direction, y , have reached equilibrium. The foregoing inequality implies $\varepsilon = a/L \ll 1$. For our calculations, it is first convenient to move into a frame travelling with the mean speed of the flow, namely $\xi = x - 2t/3$. Equations (34) and (35) are then non-dimensionalized *via* the following scalings:

$$(x, y) = (L\tilde{x}, a\tilde{y}), \quad t = \frac{L^2}{D}\tilde{t}, \quad u = U\tilde{u}, \quad \text{and} \quad \omega = \frac{U}{a}\tilde{\omega}.$$

Under these scalings, a distinguished asymptotic limit arises when $\text{Pe}_r = \varepsilon \text{Pe}$, consistent with (28). Dropping the tilde notation, the dimensionless form of equations (34) and (35) are

$$\begin{aligned} \varepsilon^3 \text{Pe}_r \frac{\partial P}{\partial t} = & -\varepsilon \text{Pe}_r \hat{u}(y) \frac{\partial P}{\partial \xi} + \varepsilon^3 \text{Pe}_r D_{xx}(\theta) \frac{\partial^2 P}{\partial \xi^2} + 2\varepsilon^2 \text{Pe}_r D_{xy}(\theta) \frac{\partial^2 P}{\partial \xi \partial y} \\ & + \varepsilon \text{Pe}_r D_{yy}(\theta) \frac{\partial^2 P}{\partial y^2} + \frac{\partial^2 P}{\partial \theta^2} - \text{Pe}_r \frac{\partial}{\partial \theta} (\omega(y, \theta) P) \end{aligned} \quad (36)$$

and

$$D_{yy}(\theta) \left. \frac{\partial P}{\partial y} \right|_{y=\pm 1} = 0, \quad (37)$$

where $\hat{u}(y) = \frac{1}{3} - y^2$.

B. The dispersion coefficient and mean particle speed

We now consider a regular perturbation expansion of P in powers of ε of the form

$$P(\mathbf{x}, \theta, t) = P^{(0)}(\mathbf{x}, \theta, t) + \varepsilon P^{(1)}(\mathbf{x}, \theta, t) + \mathcal{O}(\varepsilon^2). \quad (38)$$

At leading order, equation (36) yields,

$$\frac{\partial^2 P^{(0)}}{\partial \theta^2} - \text{Pe}_r \frac{\partial}{\partial \theta} (\omega(y, \theta) P^{(0)}) = 0. \quad (39)$$

The solution $P^{(0)}$ is decomposed multiplicatively as $P^{(0)} = g(\theta; y) C_p(\mathbf{x}, t)/N$, where g represents the orientational distribution of the particles at each shear layer, y , and C_p is the net concentration of particles at position $\mathbf{x} = (x, y)$ and time, t . Substituting this form of $P^{(0)}$ into (39), the orientational distribution, g , is determined *via* the following periodic boundary-value problem:

$$\frac{\partial^2 g}{\partial \theta^2} - \text{Pe}_r \frac{\partial}{\partial \theta} (\omega(y, \theta) g) = 0, \quad \int_0^\pi g \, d\theta = \langle g \rangle = 1, \quad (40)$$

which is solved using a truncated Fourier series of the form [27]

$$g = \frac{1}{\pi} + \sum_{n=1}^M \{a_n(y) \cos(2n\theta) + b_n(y) \sin(2n\theta)\}.$$

The differential equation (40) was imposed at discrete intervals of $\Delta\theta = \pi/N$ in the domain $\theta \in [0, \pi)$, resulting in an overdetermined, linear system of dimension $N \times 2M$ for the Fourier coefficients a_n and b_n . For each value of y , the Fourier coefficients' solution vector was found by a standard QR least-squares algorithm in MATLAB [45]. For the computations reported here, we take $N = 500$ and $M = 50$, which was found to provide more-than-sufficient accuracy.

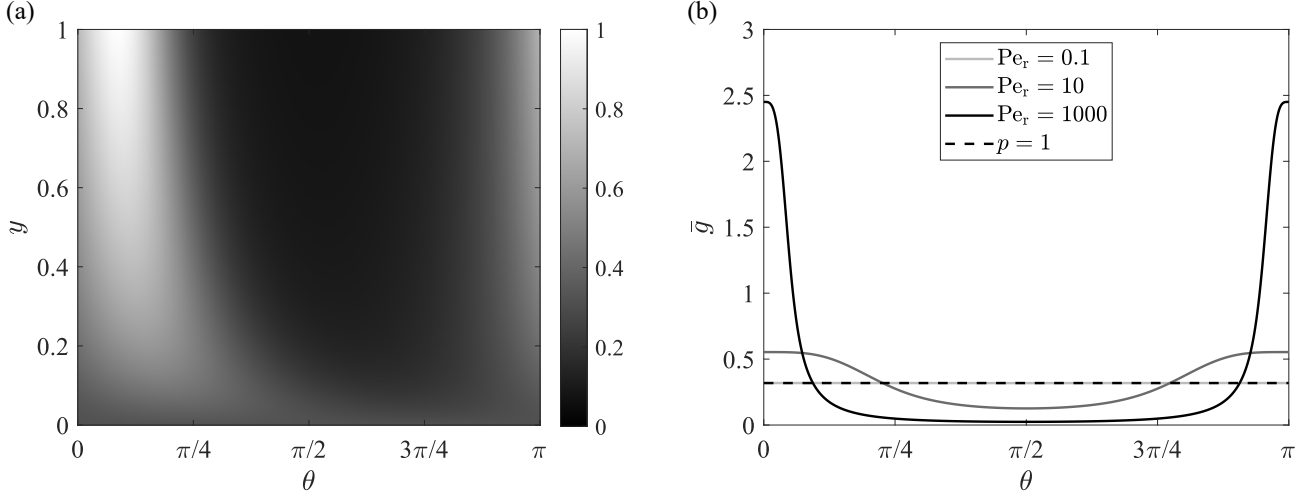


FIG. 7. (a) Plot of the orientational distribution as a density function, $g(\theta; y)$, for different values of y . Here $p = 1000$, and $\text{Pe}_r = 10$. (b) Plots of \bar{g} versus the orientation angle, θ , for different values of Pe_r and $p = 1000$. When Pe_r is small and rotational Brownian motion dominates, the orientational distribution of the particles is approximately uniform; the particles have a greater propensity to align themselves with flow as Pe_r increases. The laterally averaged orientational distribution compares well with the particles distribution from Monte Carlo simulations as seen in Figure 4(b).

In Figure 7, we plot the orientational distribution, g , for varying y and the laterally averaged orientational distribution \bar{g} for different values of the rotational Peclet number, Pe_r . We observe that as we move from a Brownian motion to shear-dominated regime, the particles have an increasing propensity to align themselves with the flow direction, consistent with the Monte Carlo simulations (Figure 4). Indeed, as $\text{Pe}_r \rightarrow \infty$, the solution to (40) develops a sharp boundary layer near $\theta = 0$, although this limit technically violates the assumptions under which the analysis is valid.

After averaging over particle orientations and applying periodicity of P , at $\mathcal{O}(\varepsilon)$ we find

$$\frac{\partial}{\partial y} \left(\langle D_{yy} g \rangle \frac{\partial C_p}{\partial y} + \left\langle D_{yy}(\theta) \frac{\partial g}{\partial y} \right\rangle C_p \right) = \hat{u}(y) \frac{\partial C_p}{\partial \xi}. \quad (41)$$

Equation (41) is a steady-state advection-diffusion equation for the concentration, C_p , in the lateral direction, y . The flux term on the left-hand side of (41) consists of an orientationally averaged diffusion coefficient and migration velocity

$$D_y(y) = \langle D_{yy} g \rangle \quad \text{and} \quad v_d(y) = \left\langle D_{yy} \frac{\partial g}{\partial y} \right\rangle = \frac{\partial D_y}{\partial y}, \quad (42)$$

respectively [27], plots of which are shown in Figure 8. Due to the form of $D_{yy}(\theta)$, the diffusion coefficient, D_y , can be written as a Fourier sine series of the form

$$D_y = \frac{1}{2} + a_2(y) \frac{\beta \pi}{2} - \sum_{n, \text{odd}} \frac{2a_n(y)}{n(n^2 - 4)} (n^2(\beta - 1) + 4) \sin\left(\frac{n\pi}{2}\right), \quad (43)$$

where

$$\beta = \frac{D_{\perp} - D_{\parallel}}{D_{\perp} + D_{\parallel}}. \quad (44)$$

As shown in Figure 8(b), particles near the center of the channel ($y = 0$) migrate towards regions of high shear ($y = \pm 1$) with a migration velocity v_d . Simultaneously, the particles close to channel walls are diffused less strongly back into the bulk as shown in Figure 8(a).

To proceed, we appeal to the assumptions stated in §III A, namely that, after sufficiently long time, $\partial C_p / \partial \xi$ is independent of y [5] and $\partial C_p / \partial \xi \approx \partial \bar{C}_m / \partial \xi$, where we recall that \bar{C}_m is the laterally averaged concentration of

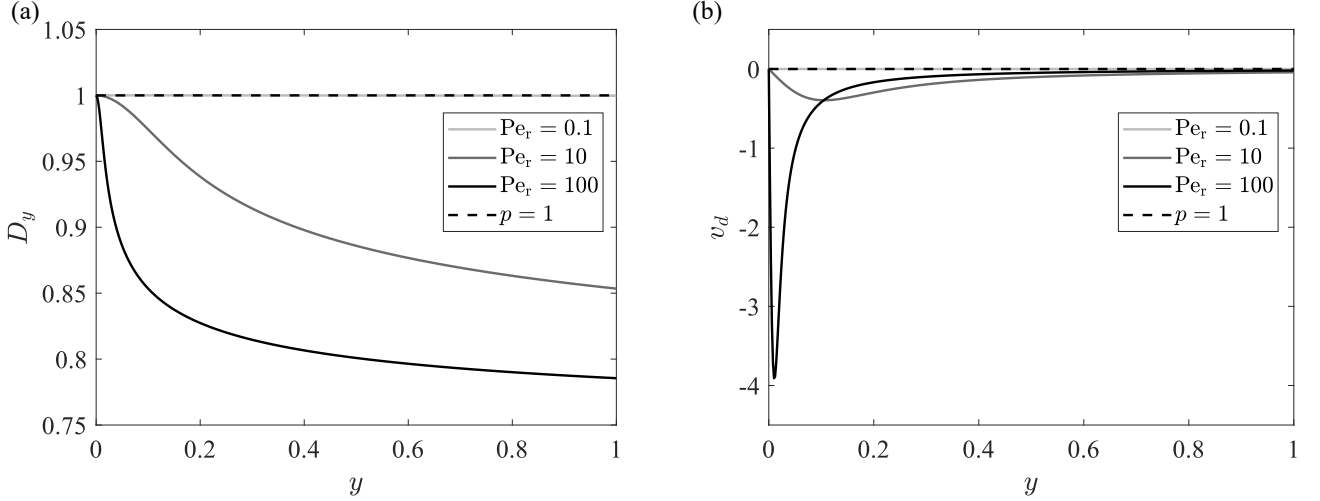


FIG. 8. Plots of (a) the orientationally averaged lateral diffusion coefficient, D_y , and (b) the lateral migration velocity, v_d , for $p = 1000$ as a function of the position along the width of the channel. As we move from a Brownian motion ($\text{Pe}_r \ll 1$) to a shear dominated regime ($\text{Pe}_r \gg 1$), the particles migrate more strongly from $y = 0$ to the channel walls, where they simultaneously experience lower diffusion back into the bulk.

solute. Under these two assumptions, equation (41) may be integrated subject to the orientationally averaged no-flux condition (37) to obtain

$$C_p = -\frac{1}{D_y} G(y) \frac{\partial \bar{C}_m}{\partial \xi} + \frac{1}{D_y} A(\xi, t) \quad \text{where} \quad G(y) = \frac{1}{6} y^2 \left(1 - \frac{1}{2} y^2 \right). \quad (45)$$

The remaining unknown constant of integration, $A(\xi, t)$, is obtained by averaging equation (45) over y to obtain

$$C_p = \frac{D_y^{-1}}{D_y^{-1}} \bar{C}_m - D_y^{-1} (G - \bar{G}) \frac{\partial \bar{C}_m}{\partial \xi} \quad \text{where} \quad \bar{G} = \frac{\int_{-1}^1 D_y^{-1} G \, dy}{\int_{-1}^1 D_y^{-1} \, dy}. \quad (46)$$

Returning to the laboratory frame, conservation of mass implies

$$\frac{\partial \bar{C}_m}{\partial t} = -\frac{\partial}{\partial x} \int_{-1}^1 u(y) C_p(x, y, t) \, dy,$$

and hence \bar{C}_m obeys the following advection-diffusion equation

$$\frac{\partial \bar{C}_m}{\partial t} + U_p \frac{\partial \bar{C}_m}{\partial x} = \kappa \frac{\partial^2 \bar{C}_m}{\partial x^2}, \quad (47)$$

where

$$U_p = \frac{\int_{-1}^1 D_y^{-1} u \, dy}{\int_{-1}^1 D_y^{-1} \, dy} \quad \text{and} \quad \kappa = -\int_{-1}^1 u(y) D_y^{-1} [G - \bar{G}] \, dy \quad (48)$$

are the mean speed of the particles and the dispersion coefficient, respectively. (For spherical particles, $p = D_y = 1$, from which it may readily be shown that $U_p = 2/3$ and $\kappa = 16/945$, consistent with equations (2) and (3).) In Figure 9(a), we plot U_p for $p \geq 1$ and various values of Pe_r , from which we infer that \bar{C}_m is dispersed relative to a frame travelling slower than the mean speed of the flow.

As shown in Figure 9(a), even for elongated particles ($p > 1$), the mean speed of the particles is approximately the mean speed of the flow ($U_p \approx 2/3$) when $\text{Pe}_r \ll 1$. As Pe_r is increased, the particles migrate towards the channel walls where the local fluid velocity is smaller. The different orientational distributions at each shear layer cause the particles to have different local D_y values which is balanced by a net lateral migration velocity, as seen in Figure 8. There is a local minimum in the mean speed of the particles around $\text{Pe}_r \approx 10$, as seen in Figure 9. Beyond $\text{Pe}_r \gtrsim 10$,

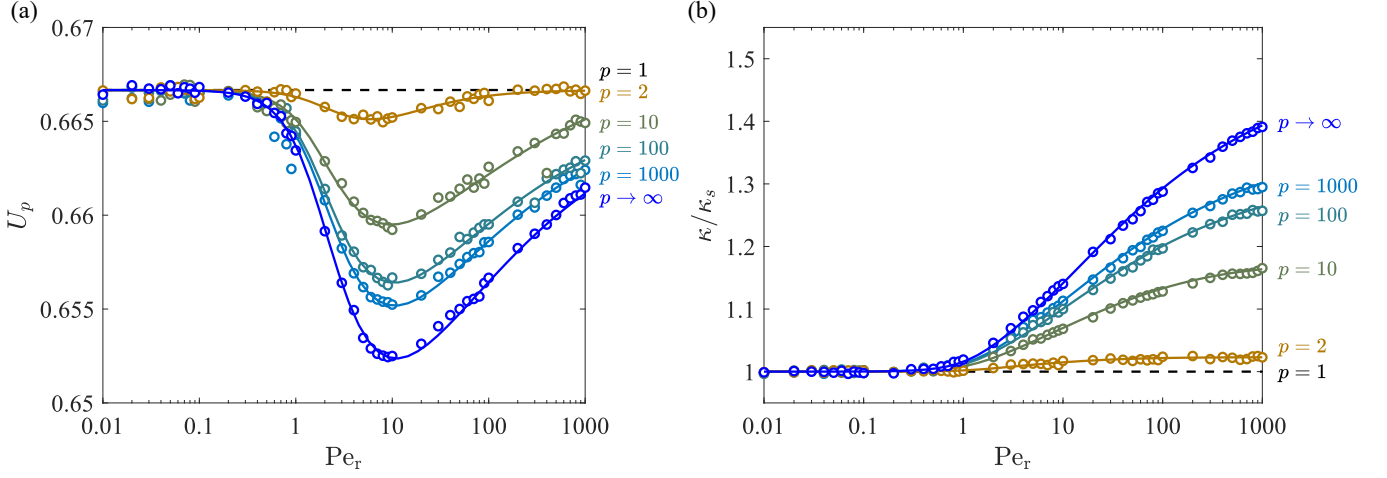


FIG. 9. Plots of (a) the mean speed of the particles, U_p , and (b) the effective dispersion, κ_m , as a function of Pe_r for different aspect ratios, p . Circles are the results of our Monte Carlo simulations, and the solid line is the theoretical estimate given by equations (48).

the orientational distributions are quite similar at each shear layer away from the center of the channel making the local diffusion constant D_y very similar across y . As a result, the overall lateral migration is actually smaller for large values of Pe_r .

As seen in Figure 9(b), the theoretical prediction and the Monte Carlo simulation shows excellent agreement. Furthermore, in Figure 10, by normalizing the dispersion factor κ with respect to its maximum possible value κ_m and minimum possible value κ_s , the curves for different p approximately collapse along one master curve. As p decreases from approximately 10 to 1, the results diverge from the master curve and approach the flat line corresponding to Taylor's case of $p = 1$. This observation suggests that in the limit of large p and large Pe , the asymptotic dispersion coefficient for elongated particles can be captured by a single curve, which depends only on Pe_r . This curve ultimately may serve as a simple and accessible correction factor to extend Taylor's result to the case of highly elongated rods.

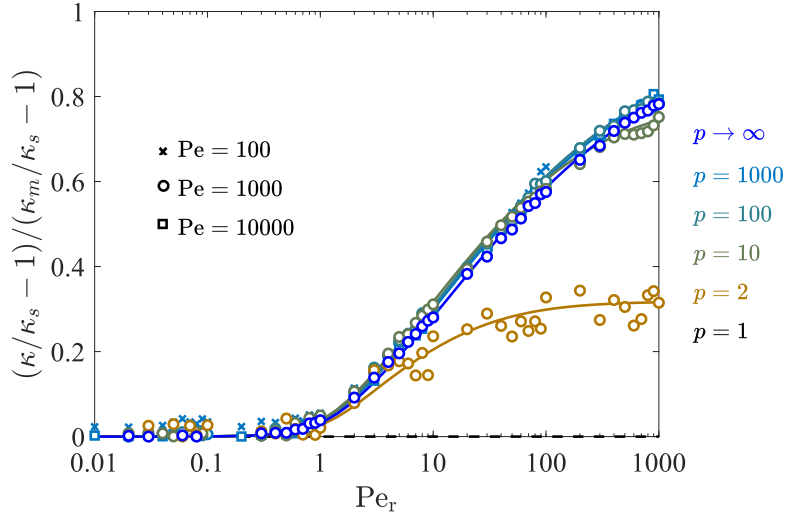


FIG. 10. The fraction of the maximum possible dispersion enhancement achieved for a rod of aspect ratio p as a function of the rotational Peclet number Pe_r . The data approximately collapses along a single curve for $p \gtrsim 10$.

IV. CONCLUSION

In this study, we have examined the dispersion factor of elongated rods in a two-dimensional pressure-driven shear flow at high Pe using Monte Carlo simulation and a simplified Taylor dispersion theory. For low Pe_r , the rods behave identically to spherical particles with similar values of the dispersion constant and mean particle speed. As the Pe_r increases, the rods align themselves more in the direction of the flow, making it more difficult for them to diffuse across the streamlines as compared to spherical particles. This reduced lateral diffusion directly results in an enhanced spreading of particles longitudinally, characterized by a larger value of the dispersion factor, as is demonstrated in Monte Carlo simulations and quantitatively captured by a simplified model inspired by Taylor's original work. Furthermore, the same theory allows us to characterize the mean speed of the particles, which always remains below the mean speed of the flow, and exhibits a distinct minimum as Pe_r is varied. Our work reveals both when the non-spherical shape of the particle has an appreciable influence on the bulk dispersion properties as well as the conditions under which an elongated particle can be safely approximated as spherical (isotropic) in application.

The present study focuses on two-dimensional flows and constrained rotational particle motion but could be extended to three-dimensional flows with unconstrained rotation. While the quantitative details will inevitably differ, we similarly expect an enhanced spreading in three-dimensional flows due to the physical mechanism of flow alignment highlighted within the present work. The subtle roles of channel geometry, more detailed particle shapes, and other more physically relevant boundary conditions on the dispersion process also deserve future attention.

ACKNOWLEDGMENTS

We acknowledge funding received from NSF through award CMMI-1634552 and from the Brown OVPR Salomon Research Award. The Monte Carlo simulations were conducted using computational resources and services at the Center for Computation and Visualization, Brown University. We would also like to thank Prof. Qian Chen and Brandon Vorrius from the Warren Alpert Medical School at Brown University for fruitful discussions helped conceive this research question.

-
- [1] T. M. Squires and S. R. Quake, Microfluidics: Fluid physics at the nanoliter scale, *Rev. Mod. Phys.* **77**, 977 (2005).
 - [2] H. A. Stone, A. D. Stroock, and A. Ajdari, Engineering flows in small devices: microfluidics toward a lab-on-a-chip, *Annu. Rev. Fluid Mech.* **36**, 381 (2004).
 - [3] T. A. Witten and H. Diamant, A review of shaped colloidal particles in fluids: Anisotropy and chirality, *Rep. Prog. Phys.* **83**, 116601 (2020).
 - [4] N. P. Truong, M. R. Whittaker, C. W. Mak, and T. P. Davis, The importance of nanoparticle shape in cancer drug delivery, *Expert Opin. Drug Del.* **12**, 129 (2015).
 - [5] G. I. Taylor, Dispersion of soluble matter in solvent flowing slowly through a tube, *Proc. Roy. Soc. A-Math. Phys.* **219**, 186 (1953).
 - [6] R. Aris, On the dispersion of a solute in a fluid flowing through a tube, *Proc. Roy. Soc. A-Math. Phys.* **235**, 67 (1956).
 - [7] I. Frankel and H. Brenner, On the foundations of generalized Taylor dispersion theory, *J. Fluid Mech.* **204**, 97 (1989).
 - [8] N. Hill and M. Bees, Taylor dispersion of gyrotactic swimming micro-organisms in a linear flow, *Phys. Fluids* **14**, 2598 (2002).
 - [9] A. Manela and I. Frankel, Generalized Taylor dispersion in suspensions of gyrotactic swimming micro-organisms, *J. Fluid Mech.* **490**, 99 (2003).
 - [10] W. Jiang and G. Chen, Dispersion of active particles in confined unidirectional flows, *J. Fluid Mech.* **877**, 1 (2019).
 - [11] W. Jiang and G. Chen, Dispersion of gyrotactic micro-organisms in pipe flows, *J. of Fluid Mech.* **889** (2020).
 - [12] Z. Peng and J. F. Brady, Upstream swimming and Taylor dispersion of active Brownian particles, *Phys. Rev. Fluids* **5**, 073102 (2020).
 - [13] A. Dehkharghani, N. Waisbord, J. Dunkel, and J. S. Guasto, Bacterial scattering in microfluidic crystal flows reveals giant active Taylor-Aris dispersion, *Proc. Natl. Acad. Sci. USA* **116**, 11119 (2019).
 - [14] D. Dutta, A. Ramachandran, and D. T. Leighton, Effect of channel geometry on solute dispersion in pressure-driven microfluidic systems, *Microfluid. Nanofluid.* **2**, 275 (2006).
 - [15] M. Aminian, F. Bernardi, R. Camassa, D. M. Harris, and R. M. McLaughlin, How boundaries shape chemical delivery in microfluidics, *Science* **354**, 1252 (2016).
 - [16] F. Bernardi, *Space/Time Evolution in the Passive Tracer Problem*, Ph.D. thesis, University of North Carolina, Chapel Hill (2018).
 - [17] S. Marbach and K. Alim, Active control of dispersion within a channel with flow and pulsating walls, *Phys. Rev. Fluids* **4**, 114202 (2019).

- [18] L. Salerno, G. Cardillo, and C. Camporeale, Aris-taylor dispersion in the subarachnoid space, *Physical Review Fluids* **5**, 043102 (2020).
- [19] Y. Han, A. M. Alsayed, M. Nobili, J. Zhang, T. C. Lubensky, and A. G. Yodh, Brownian motion of an ellipsoid, *Science* **314**, 626 (2006).
- [20] Y. Han, A. Alsayed, M. Nobili, and A. G. Yodh, Quasi-two-dimensional diffusion of single ellipsoids: Aspect ratio and confinement effects, *Phys. Rev. E* **80**, 011403 (2009).
- [21] A. Chakrabarty, A. Konya, F. Wang, J. V. Selinger, K. Sun, and Q.-H. Wei, Brownian motion of boomerang colloidal particles, *Phys. Rev. Lett.* **111**, 160603 (2013).
- [22] U. Agarwal, A. Dutta, and R. Mashelkar, Migration of macromolecules under flow: the physical origin and engineering implications, *Chem. Eng. Sci.* **49**, 1693 (1994).
- [23] R. L. Schiek and E. S. Shaqfeh, Cross-streamline migration of slender Brownian fibres in plane poiseuille flow, *J. Fluid Mech.* **332**, 23 (1997).
- [24] R. M. Jendrejack, D. C. Schwartz, J. J. De Pablo, and M. D. Graham, Shear-induced migration in flowing polymer solutions: Simulation of long-chain DNA in microchannels, *J. Chem. Phys.* **120**, 2513 (2004).
- [25] M. Makino and M. Doi, Migration of twisted ribbon-like particles in simple shear flow, *Phys. Fluids* **17**, 103605 (2005).
- [26] H. C. Fu, T. R. Powers, R. Stocker, *et al.*, Separation of microscale chiral objects by shear flow, *Phys. Rev. Lett.* **102**, 158103 (2009).
- [27] L. C. Nitsche and E. Hinch, Shear-induced lateral migration of Brownian rigid rods in parabolic channel flow, *J. Fluid Mech.* **332**, 1 (1997).
- [28] H. C. Berg, *Random walks in biology* (Princeton University Press, 1993).
- [29] H. Brenner, Coupling between the translational and rotational Brownian motions of rigid particles of arbitrary shape I. Helicoidally isotropic particles, *J. Coll. Sci. Imp. U. Tok.* **20**, 104 (1965).
- [30] H. Brenner, Coupling between the translational and rotational Brownian motions of rigid particles of arbitrary shape: II. General theory, *J. Colloid Interf. Sci.* **23**, 407 (1967).
- [31] W. A. Wegener, Diffusion coefficients for rigid macromolecules with irregular shapes that allow rotational-translational coupling, *Biopolymers* **20**, 303 (1981).
- [32] F. Perrin, Brownian motion of an ellipsoid—II. Free rotation and fluorescence depolarization. Translation and diffusion of ellipsoidal molecules, *J. Phys. Radium* **VII**, 1 (1936).
- [33] J. Happel and H. Brenner, *Low Reynolds number hydrodynamics: with special applications to particulate media*, Vol. 1 (Springer Science & Business Media, 2012).
- [34] F. Perrin, Brownian motion of an ellipsoid—I. Dielectric dispersion for ellipsoidal molecules, *J. Phys. Radium* **V**, 497 (1934).
- [35] S. Koenig, Brownian motion of an ellipsoid. A correction to Perrin's results, *Biopolymers* **14**, 2421 (1975).
- [36] G. B. Jeffery, The motion of ellipsoidal particles immersed in a viscous fluid, *Proc. Roy. Soc. A-Math. Phys.* **102**, 161 (1922).
- [37] F. P. Bretherton, The motion of rigid particles in a shear flow at low reynolds number, *J. Fluid Mech.* **14**, 284 (1962).
- [38] L. Leal and E. Hinch, The effect of weak Brownian rotations on particles in shear flow, *J. Fluid Mech.* **46**, 685 (1971).
- [39] B. D. Leahy, X. Cheng, D. C. Ong, C. Liddell-Watson, and I. Cohen, Enhancing rotational diffusion using oscillatory shear, *Phys. Rev. Lett.* **110**, 228301 (2013).
- [40] B. D. Leahy, D. L. Koch, and I. Cohen, The effect of shear flow on the rotational diffusion of a single axisymmetric particle, *J. Fluid Mech.* **772**, 42 (2015).
- [41] V. G. Kulkarni, *Modeling and analysis of stochastic systems* (Crc Press, 2016).
- [42] B. Lapeyre, É. Pardoux, E. Pardoux, and R. Sentis, *Introduction to Monte Carlo methods for transport and diffusion equations*, Vol. 6 (Oxford University Press on Demand, 2003).
- [43] P. E. Kloeden, E. Platen, and H. Schurz, *Numerical solution of SDE through computer experiments* (Springer Science & Business Media, 2012).
- [44] H. Brenner and D. W. Condiff, Transport mechanics in systems of orientable particles. IV. Convective transport, *J. Colloid Interf. Sci.* **47**, 199 (1974).
- [45] L. N. Trefethen and D. Bau III, *Numerical linear algebra*, Vol. 50 (Siam, 1997).